Tritium Science Program FY23 project Report:

First-Principles Studies of Tritium Species Dissociability & Diffusivity Across the Interface of Nickel-Plated Zircaloy-4

De Nyago Tafen[1,3], Morgan Redington[2], Hari P. Paudel[2,4], and Yuhua Duan[2]

[1]U.S. Department of Energy, National Energy Technology Laboratory, 1450 Queen Avenue SW, Albany, OR 97321 USA

[2]U.S. Department of Energy, National Energy Technology Laboratory, 626 Cochran Mill Road, Pittsburgh, PA 15236-0940, USA

[3]NETL Support Contractor, 1450 Queen Avenue SW, Albany, OR 97321 USA

[4]NETL Support Contractor, 626 Cochran Mill Road, Pittsburgh, PA 15236-0940, USA

DOE/NETL-2023/3931. December 28, 2023

U.S. DEPARTMENT OF ENERGY | NATIONAL ENERGY TECHNOLOGY LABORATORY

Disclaimer

This project was funded by the United States Department of Energy, National Energy Technology Laboratory, in part, through a site support contract. Neither the United States Government nor any agency thereof, nor any of their employees, nor the support contractor, nor any of their employees, makes any warranty, express or implied, or assumes any legal liability or responsibility for the accuracy, completeness, or usefulness of any information, apparatus, product, or process disclosed, or represents that its use would not infringe privately owned rights. Reference herein to any specific commercial product, process, or service by trade name, trademark, manufacturer, or otherwise does not necessarily constitute or imply its endorsement, recommendation, or favoring by the United States Government or any agency thereof. The views and opinions of authors expressed herein do not necessarily state or reflect those of the United States Government or any agency thereof.

Table of Contents

List of Figures

List of Tables

1 INTRODUCTION

1.1 Project Technical Scope

Zirconium (Zr) and its alloys (Zircaloy-4) are widely used in nuclear reactors due to their low neutron adsorption cross-section and excellent corrosion resistance. In tritium-producing burnable absorber rods (TPBARs), the metal getter tube located between the cladding and the γ-$LiAlO_2$ pellets is composed of nickel (Ni)-plated Zircaloy-4, which is used to capture tritium (^3H) species (mainly $^3H_2$ and ^3H_2O) generated from γ-$LiAlO_2$ pellets during irradiation. The ^3H-related products transfer to the surface of metal Ni upon adsorption and dissociation to form new ^3H species and diffuse into the Zircaloy-4 getters to form metal hydrides (Zr^3H_x). Therefore, exploring ^3H species ($^3H_2$, ^3H_2O) dissociation on the surface of Ni and diffusion across the interface of Ni-plated Zircaloy-4 getters can provide a better understanding of ^3H species formation and transport from pellets into the getters.

In FY17-20, NETL conducted a series of studies on γ-$LiAlO_2$ pellets to understand the tritium products and their transport through the pellets [1-4]. Aside from studying the surface properties of γ-$LiAlO_2$, we also explored the diffusion of ^3H and O^3H species on its defective (100) and (101) surfaces, and the ^3H_2O formation and desorption from the γ-$LiAlO_2$ (101) and $LiAl_5O_8$ (111) surfaces [5-10]. In conclusion, we found that the $^3H_2$ molecule is the main product initially released from the pellets. With increasing the number of Li vacancies and ^3H atoms under irradiation, ^3H_2O can be formed and released from the pellets as well. In FY21-22, we explored ^3H diffusion in different zirconium hydrides [11-13]. However, there are remained open questions that need the answer: (i) how and which ^3H species (^3H, O^3H, O, or $^3H_2$, etc.) diffuse into zircaloy-4 from the

surface of γ-$LiAlO_2$ pellets? (ii) In the case of ^3H_2O, can Ni coating layer retain O by forming NiO_x or $Ni(O^3H)_x$ to prevent O diffusion into Zircalory-4 getter?

In TPBARs, $^3H_2$ and ^3H_2O molecules generated from the γ-$LiAlO_2$ pellets [5-10] are transported to the Ni-plated Zircaloy-4 getters. To fully address aforementioned open questions, in FY23, we propose to explore the $^3H_2$ and ^3H_2O molecules' dissociation on the surfaces of Ni-plated Zircaloy-4 getters to clarify which ^3H species can dissolve into the metal getters, and to calculate the diffusion pathways of these ^3H species in the bulk Ni phase to identify which species will diffuse across the interface of Ni-plated Zircalory-4. In the case of ^3H_2O, we also propose to explore the possibility of the nickel oxide/hydroxide (NiO_x, $Ni(O^3H)_x$) phase formation in the Ni-coating layer to prevent O diffusion into the zircaloy-4 getter and to calculate the diffusion pathways of ^3H across such oxide/hydroxide layer into the zircaloy-4 getter.

Since the Zircaloy-4 getter is plated by Ni magnetic metal, the Ni metal bulk and surface as well as the Ni-Zircaloy-4 interface will be our main targets in this study. In the literature, there are comprehensive studies of H_2 and H_2O adsorption on the surfaces of Ni [14, 15]. We will collect these information and briefly explore the dissociation mechanism of $^3H_2$ and ^3H_2O molecules on the most stable (111) surface of Ni to clarify which ^3H species are generated from the $^3H_2$ and ^3H_2O dissociation on the surface. Then, the possibility of ^3H species diffusion through the Ni metal will be determined to show which form of ^3H species can pass through the Ni to the interface of Ni-plated Zircaloy-4. Particularly, we want to know if O from ^3H_2O can be retained in the Ni layer to form the $NiO_x/Ni(O^3H)_x$ phase and only let ^3H diffuse to the zircaloy-4 getter to form hydrides. Finally, an interface model of Ni and Zircaloy-4 will be built for further exploration of the ^3H species diffusion with impurities across the interface and dissolution into the Zircaloy-4 getter.

Since the zirconium alloys used in TPBARs are pure and can almost be regarded as single-component systems — such as Zricaloy-4 with small alloying elements of Sn (< 2%) and Fe (< 1%) — the Zr metal will be used to build the interface of Ni and Zircaloy-4. The impurities (Sn, Fe, Ni, etc.) will be introduced in the simulation model at later time. Through this study, we expect to obtain the $^3H_2$ and ^3H_2O dissociation on the Ni (111) surface and diffusion mechanism in the Ni coated layer and the dominant ^3H species dissolution into the Zircaloy-4 getter. To achieve the objectives, we will perform the proposed investigation by using spin-polarized density functional theory (DFT) methods to capture the effects of Ni magnetic properties on ^3H diffusion. The study will use NETL supercomputer resources and does not require the use of classified data or hardware. This project was divided into four subtasks:

- **Task 1**: Exploring $^3H_2$ and ^3H_2O binding sites and their dissociation on the (111) surface of Ni. Based on available literature data, we will obtain the dissociation energy according to the possible dissociation step of $^3H_2O \rightarrow O^3H + {}^3H \rightarrow O + {}^3H + {}^3H$, $^3H_2O \rightarrow O + {}^3H_2$ and $^3H_2 \rightarrow {}^3H + {}^3H$.
- **Task 2**: Determining the ^3H species dissolve from surface into Ni bulk. For those dissociated species from Task 1, we calculate their diffusion barriers from surface to the bulk to identify the most possible ^3H species that can be dissolved into Ni metal, and verify if NiO_x or $Ni(O^3H)_x$ phase can be formed.
- **Task 3**: Identifying the energy barrier of ^3H species diffusion in the Ni bulk. Based on the ^3H species dissolved into Ni metal and the formation of NiO_x or $Ni(O^3H)_x$ phase from Task 2, we will calculate the energy barriers of ^3H species diffusion in Ni bulk (with NiO_x or $Ni(O^3H)_x$) to determine which ^3H species can get through the Ni coating to reach the Ni-Zircalory-4 interface.

- **Task 4**: Build the interface of Ni and Zr metal. We will create possible Ni-Zr interface and clarify the most stable configuration for further study (FY24) of ^{3}H species diffusion across the interface and then dissolution into Zircaloy-4 getter to form metal hydrides.

1.2 Deliverables

Publications

- H. P. Paudel, T. Jia, W. A. Saidi, D. J. Senor, A. M. Casella, Y. Duan, "*Study of Tritium Diffusivity in Pure and Sn Defective Zr: A First Principles Density Functional Theory Approach*", **J. Phys. Chem. C 127**(26)(2023)12435-12443. doi: 10.1021/acs.jpcc.3c01200.
- H. P. Paudel, C. M. Andolina, W. A. Saidi, Y. Duan, *"Developing Machine-Learning Potentials to Study Properties of the Tritium Formation and Diffusivity in Pure and Defective Zircaloy-4 Getters"*, **Tritium Science Program FY22 Final Report**, DOE/NETL-2022-3351, Jan. 2023. doi: 10.2172/1959358
- D. N. Tafen, H. P. Paudel, D. J. Senor, A. M. Casella, Y. Duan, "*Solubility and Diffusivity of Tritium Species in Interface of Nickel-Plated Zircaloy-4: First Principles Density Functional Study*", under preparation (2023)
- M. Redington, H. P. Paudel, D. N. Tafen, Y. Duan, "*Tritium Adsorption on Surfaces of Pure and Tin-Defective Zirconium*", under preparation (2023).

Presentations

- Y. Duan, T. Jia, H. P. Paudel, Y.-L. Lee, D. J. Senor, A. Casella, "*First-principles study of the tritium diffusion and formation in γ-$LiAlO_2$ pellets and Zircalory-4 getter*", **TechConnect World Innovation Conference & Expo**, June 19-21, 2023, Washington DC.
- D. N. Tafen, H. Paudel, Y. Duan, M. Redington, "*First-Principles Studies of Tritium Species Dissociability and Diffusivity Across the Interface of Nickel-Plated Zircaloy-4*", **8th Annual Tritium Science Technical Exchange**, September 26-27, 2023, Pacific Northwest National Laboratory, Richland, WA.

1.3 Organization of the Report

We organize this report as follow. We present theoretical and computational methodologies implemented in this work in the chapter 2. In chapter 3 we present and discuss the results of our study. In chapter 4 we give a brief summary and conclusion.

2 THEORETICAL AND COMPUTATIONAL METHODS

All the calculation were performed based on density functional theory (DFT) with the plane-wave basis set and the pseudopotential as implemented in the Vienna ab initio simulation package (VASP) [16-18]. The electron-ion interaction is described with the projector augmented wave method (PAW) [19, 20]. In our calculations, the potential of the isotope ^{3}H is obtained by modifying the mass in the standard ^{1}H potential. The exchange and correction energies are described within generalized gradient approximation using the spin-polarized Perdew-Burke-Ernzerhof formulation (GGA-PBE) [21]. A cutoff energy of 400 eV was used for the plane wave expansion. The convergence criteria for geometry optimizations of total energy and force were 10^{-5} eV and 0.01 eV/Å, respectively.

The surface slab was generated from the fully relaxed bulk structure. For the Ni(111) surfaces we used a five-layered 4 × 4 supercell slab with a vacuum region of 12 Å along the z-axis. The k-point sampling in a reciprocal space was generated using Monkhorst-Pack method and a 3 × 3 × 1 grid size.

Diffusion barriers for reactions were calculated using the climbing nudged elastic band (c-NEB) method [22]. For each simulation we used a minimum of five images. The energy difference between the two optimized minima gives the reaction energy.

3 RESULTS AND DISCUSSION

3.1 Exploring $^3H_2$ and ^3H_2O binding sites and their dissociation on the (111) surface of Ni.

We explore the $^3H_2$ and ^3H_2O molecules' dissociation on the surfaces of Ni-plated Zircaloy-4 getters represented here by Ni(111) surface to clarify which ^3H species can dissolve into the metal getters, and to calculate the diffusion pathways of these ^3H species in the bulk Ni phase to identify which species will diffuse across the interface of Ni-plated Zircalory-4. Based on the literature data, ^3H_2O molecules will dissociate on Ni(111) according to the following mechanism:

$^3H_2O \rightarrow O^3H + {}^3H$ and $O^3H + {}^3H \rightarrow O + {}^3H + {}^3H$

The first dissociation requires an activation energy of 0.68 eV where ^3H_2O is dissociated into an O^3H and ^3H species [23]. The second process involves the dissociation of O^3H into O and ^3H and requires a higher activation barrier of 1.25 eV [23]. The ^3H_2O species will adsorbed on Ni(111) by occupying a top of a Ni atom, whereas the other three species, O^3H, ^3H, and O, will occupy a 3-fold hollow site fcc.

As $^3H_2$ reaches Ni(111) surface it can dissociate into two atomic ^3H ($^3H_2 \rightarrow {}^3H + {}^3H$) with a low activation energy. For example, Shirazi et al. obtained activation energies of 0.03 and 0.09 eV for H-coverage of 0.125 and 0.25 monolayer (ML), respectively [24].

Having determine the mechanisms of dissociation of ^3H_2O and ^3H_2O molecules on nickel surface we turn our attention into the diffusion of the above species into the Ni bulk phase and a possible formation of NiO_x and/or $Ni(OH)_x$ phase.

3.2 Stability and formation of NiO_x and/or $Ni(OH)_x$ phase

The stability of Ni metal and its derived compounds, including oxides, hydroxides, and oxyhydroxides can be readily predicted from DFT combined with thermodynamic analysis. To predict the stability and formation of NiO_x and/or $Ni(OH)_x$ phase, we will limit ourselves to the most stable compounds of nickel oxides, hydroxides and oxyhydroxides observed experimentally (Table 1). We computed the equilibrium crystal structures, electronic structures, and thermodynamic energies using density functional theory with different flavors of exchange correlation potentials. In addition to the PBE functional, we used the hybrid functional HSE06 [25] and a PBE+U functional. The HSE06 tends to perform better especially when dealing with oxides. Electronic structures and thermodynamic analysis are combined together to determine the chemical potential domains of $Ni(OH)_x$ stability and phase formation.

3.2.1 Calculations of total and formation energies

The formation energy of a $Ni_xO_yH_z$ compound can be defined as follows:

$$\Delta H(Ni_xO_yH_z) = E_{DFT}(Ni_xO_yH_z) - x\mu_{Ni}^{solid} - y\mu_O^{gas} - z\mu_H^{gas} \quad (1)$$

where $E_{DFT}(Ni_xO_yH_z)$ is the DFT calculated total energy of the compound; μ_{Ni}^{solid}, μ_O^{gas}, and μ_H^{gas} are the chemical potentials of Ni, O, and H in their stable elemental solid/gas state; x, y, and z are coefficients of proportionality. In Table 1, we listed the DFT calculated total and formation energies of the most stable compounds of nickel oxides and hydroxides using different flavors of exchange correlation functionals. The formation energy ΔH for the PBE corrected and PBE+U corrected used a corrected value for the O_2 molecule. Our results for the formation energies are in good agreement with literature data [26, 27]. The computed total energies and formation energies

of these compounds are used to determine the chemical potential domains for the formation of $Ni(OH)_x$.

Table 1. Space groups, calculated total and formation energies (eV/f.u.) of Ni-O-H based compounds.

Compound	Space group	Formula unit	Total energy HSE06	Total energy PBE	Total energy PBE+U	ΔH HSE06	ΔH PBE	ΔH PBE corrected	ΔH PBE+U corrected
Ni	Fm-3m	1	-6.448	-5.459	-1.842				
H_2		1	-7.713	-6.772	-6.772				
O_2		1	-17.036	-9.862	-9.862				
NiO	Fm-3m	2	-17.970	-11.655	-10.278	-3.004	-1.265	-1.945	-4.184
NiO_2	P-3m1	1	-25.491	-17.350	-14.277	-2.007	-2.029	-3.389	-3.933
Ni_2O_3	R-3c	2	-42.851	-29.648	-24.132	-4.402	-3.937	-5.977	-7.694
Ni_3O_4	Fd-3m	8	-61.366	-41.783	-34.696	-7.950	-5.681	-8.401	-12.165
$Ni(OH)_2$	P-3m1	1	-37.451	-26.220	-25.071	-6.255	-4.127	-5.487	-7.955
NiOOH	R-3m	2	-31.462	-22.124	-19.789	-4.122	-3.417	-4.777	-6.059

3.2.2 Chemical potential domains for the stability and formation of $Ni(OH)_2$

The formation and stability of a system depend on the chemical potential of its constituent elements, which varies with specific equilibrium conditions. In the thermodynamic limits, the chemical potential domains for $Ni(OH)_2$ can be determined. The stability of $Ni(OH)_2$ against decomposition into its elemental constituents requires a smaller atomic chemical potential than the corresponding elemental solid, i.e.,

$$\mu_i \leq \mu_i^{solid/gas}, i = Ni, H, O. \quad (2)$$

Setting $\Delta\mu_i = \mu_i - \mu_i^{solid/gas}$, the above condition becomes

$$\Delta\mu_i \leq 0, \qquad i = Ni, H, O. \quad (3)$$

For $\Delta\mu_i = 0$ we obtain a maximum i-rich condition. Thermodynamic equilibrium of a system requires that a sum of the chemical potentials of its constituent atoms be equal to its formation energy. Therefore, we can write:

$$\Delta\mu_{Ni} + 2\Delta\mu_O + 2\Delta\mu_H = \Delta H(Ni(OH)_2) \quad (4)$$

where $\Delta H(Ni(OH)_2)$ is the formation energy of bulk $Ni(OH)_2$.

To avoid the formation of other oxide compounds, the ranges of chemical potentials are subject to the following additional criteria:

$$\Delta\mu_{Ni} + \Delta\mu_O \leq \Delta H(NiO) \quad (5)$$

$$\Delta\mu_{Ni} + 2\Delta\mu_O \leq \Delta H(NiO_2) \quad (6)$$

$$2\Delta\mu_{Ni} + 3\Delta\mu_O \leq \Delta H(Ni_2O_3) \quad (7)$$

$$3\Delta\mu_{Ni} + 4\Delta\mu_O \leq \Delta H(Ni_3O_4) \quad (8)$$

$$\Delta\mu_{Ni} + 2\Delta\mu_O + \Delta\mu_H \leq \Delta H(NiOOH) \quad (9)$$

Combining Eq. 4 and 5-9 we computed the chemical potential domains for the formation and stability of $Ni(OH)_2$ using the total energies and formation energies calculated above. Figure 1 shows the stable chemical potential region of the bulk $Ni(OH)_2$ in terms of the chemical potentials $\Delta\mu_O, \Delta\mu_{Ni}$, and $\Delta\mu_H$ using PBE and HSE06 functionals. In the PBE functional the limiting stable conditions are defined by five points namely A(-4.13, 0, 0), B(-2.71, 0, -0.71), C(-0.27, -1.22, -0.71), D(0, -1.42, -0.64), and E(0, -2.06, 0) with boundary lines formed by Ni(OH)2, NiOOH and Ni_3O_4. In contrast the limiting stable conditions using the HSE06 functional is defined by the following four points A(-6.26, 0, 0), B(-3.00, 0, -1.63), C(0, -3.00, -0.12), and D(0, -3.13, 0) with boundary lines corresponding to $Ni(OH)_2$ and NiO.

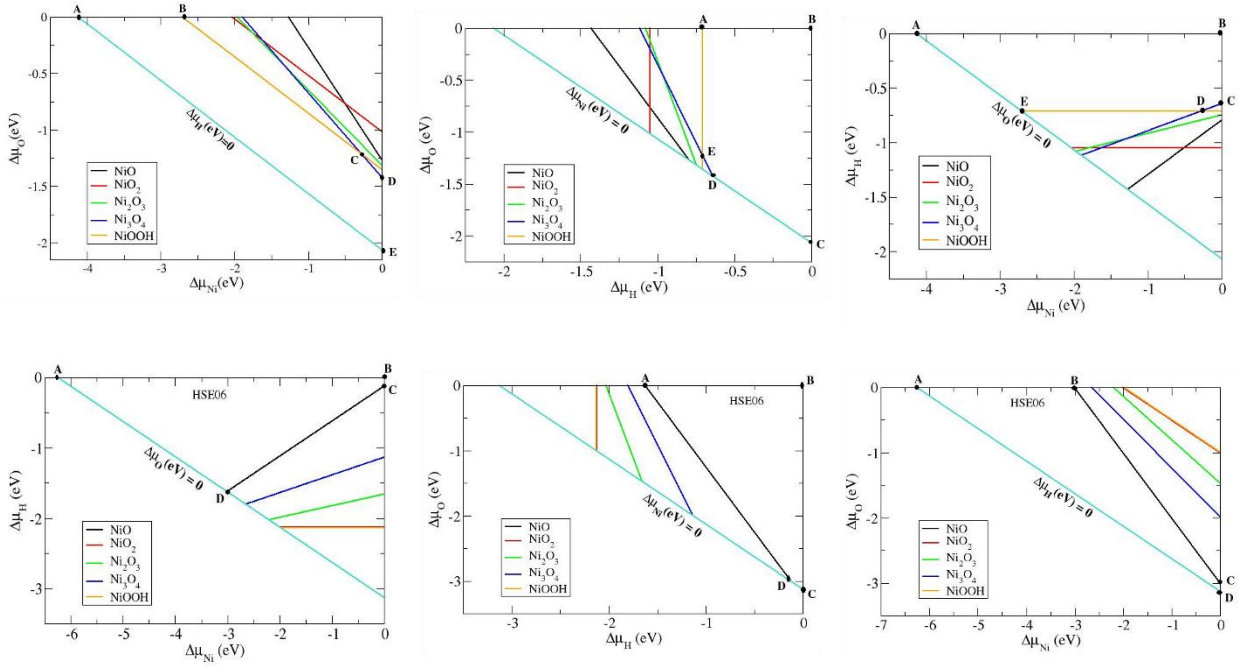

Figure 1. The allowed chemical potential domains (regions determined by A, B, C, D, and E) for $Ni(OH)_2$ to be stable. Top: results obtained using PBE functional. Bottom: results obtained using HSE06 functional. The secondary phases which are indicated by color-coded lines restrict the stable phase.

To understand the discrepancy between the results from the PBE and HSE06 functionals, we look at the formation energy per atom for nickel oxide compounds. In Figure 2, we compare the formation energy per atom of the oxide compounds obtained using PBE, HSE06, and PBE+U functionals. The results show that HSE06 correctly predict NiO as the most stable among all Ni oxides in agreement with experiments whereas PBE incorrectly assigns the lowest formation energy to Ni_3O_4. PBE+U follows the same trend as HSE06. Our results also show that the formation energy per atom of $Ni(OH)_2$ is lower than that of NiOOH in HSE06 (-1.25 eV/at vs. -1.03 eV/at), but it is the reverse in PBE (-0.82 eV/at vs. -0.85 eV/at). Overall the chemical potential domains are better described using HSE06 functional.

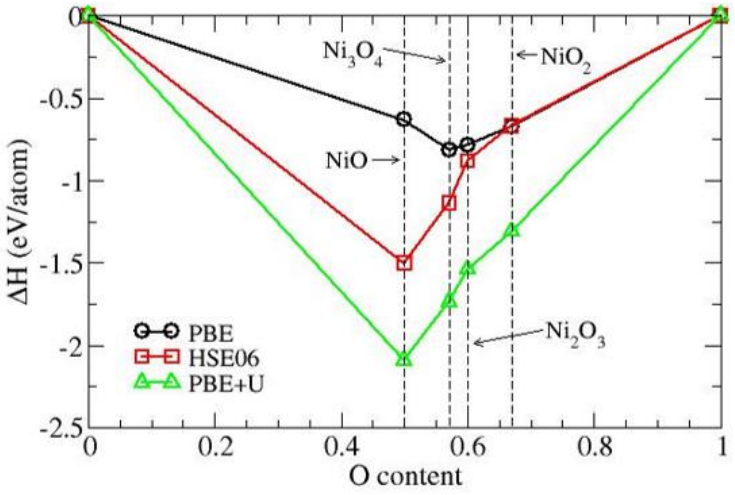

Figure 2. Formation energies per atom from PBE, HSE06, and PBE+U functionals for nickel oxide compounds.

3.3 Determining the ^{3}H species dissolve from surface into Ni bulk

3.3.1 Tritium (^{3}H) diffusion from Ni(111) surface to bulk

For our based line we first calculated the diffusion of a single H atom into a pure Ni(111) surface. H species will diffuse through the surface and occupy an interstitial site in the subsurface. There are two possible interstitial sites in bulk nickel: a tetrahedral (denoted as tetra) site and an octahedral (denoted as octah) site. Figure 3 shows the migration of H species from the surface into bulk. The calculated migration barrier of H from an fcc surface to a subsurface octahedral is 0.698 eV. This reaction is endothermic by 0.621 eV. H species on a subsurface octahedral can diffuse into the bulk via a tetrahedral site with an activation energy of 0.454 eV.

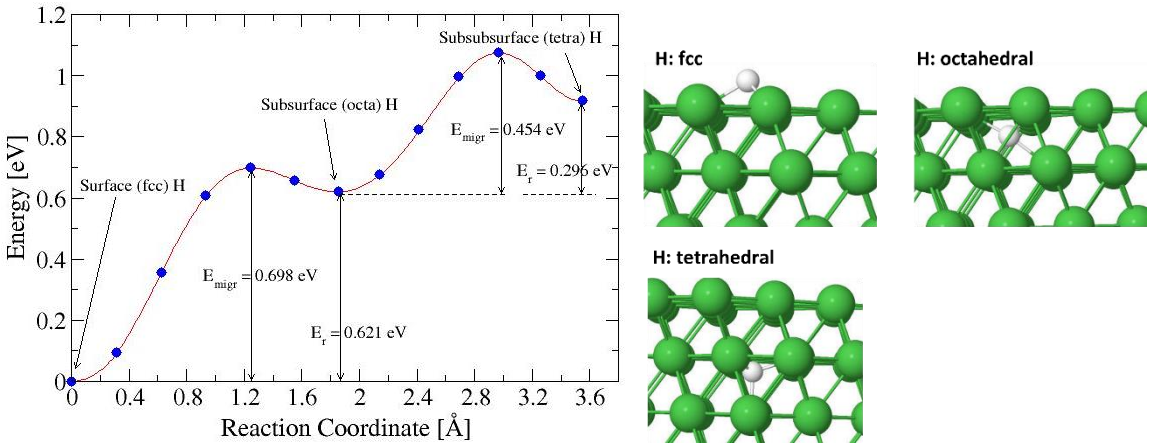

Figure 3. Energy barrier and transition pathway for H diffusing into a pure Ni(111) surface.

3.3.2 Migration of ^{3}H species from surface to subsurface after $^{3}H_2O$ dissociation

Next we investigated the diffusion of H into the surface after a H_2O dissociation. We looked at both cases: partial and complete dissociation. In the partial dissociation, we have an H and OH species on the surface. In complete dissociation we have two H species and an O species on the surface. Our results show a lower H diffusion barrier in the case of a complete dissociation compared to that in the partial dissociation (Figure 4).

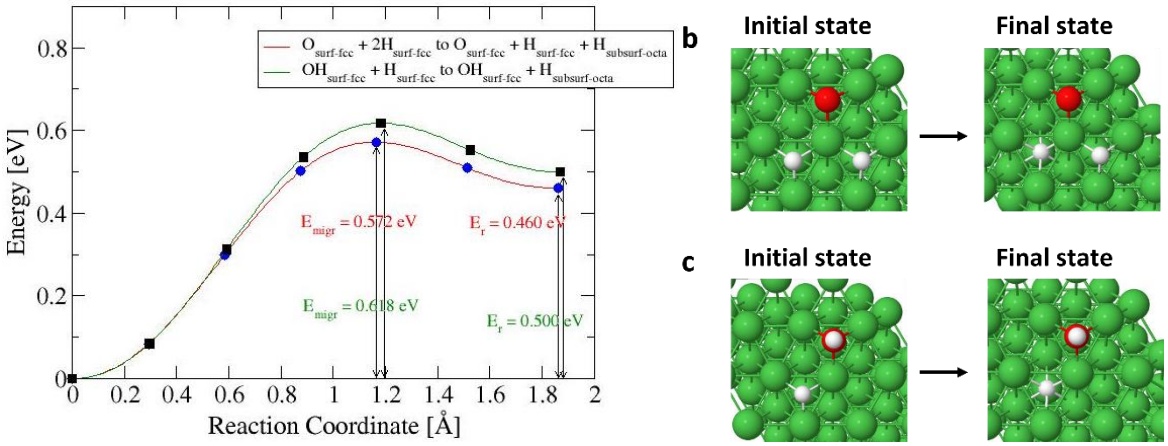

Figure 4. Energy barrier of ^{3}H species migration from surface to subsurface after $^{3}H_2O$ dissociation. Structures of the initial and final states.

3.3.3 Migration of O species from surface to subsurface

The migration of O species from a fcc surface site to a subsurface octahedral requires the presence of a defect such as Ni vacancy. Our study reveals that in the absence of Ni vacancy O diffusion into the surface is unfavorable. We studied the diffusion of O species in a pure Ni surface with a subsurface Ni vacancy (Ni_v) and the diffusion of O after an H_2O dissociation (Figure 5). Our calculations reveal that it is easier for O to diffuse into the surface in the presence of H species than an O diffusing through a pure Ni(111) surface. In the presence of H species the activation energy and reaction energy are 1.341 eV and 1.226 eV, respectively, compared to 1.574 eV and 1.510 eV for pure Ni surface with a subsurface Niv.

Compared to H species, O species requires higher barriers to diffuse into Ni surface. Therefore, it will be more favorable for H to pass through the nickel coating and reach the Ni-Zircalory-4 interface.

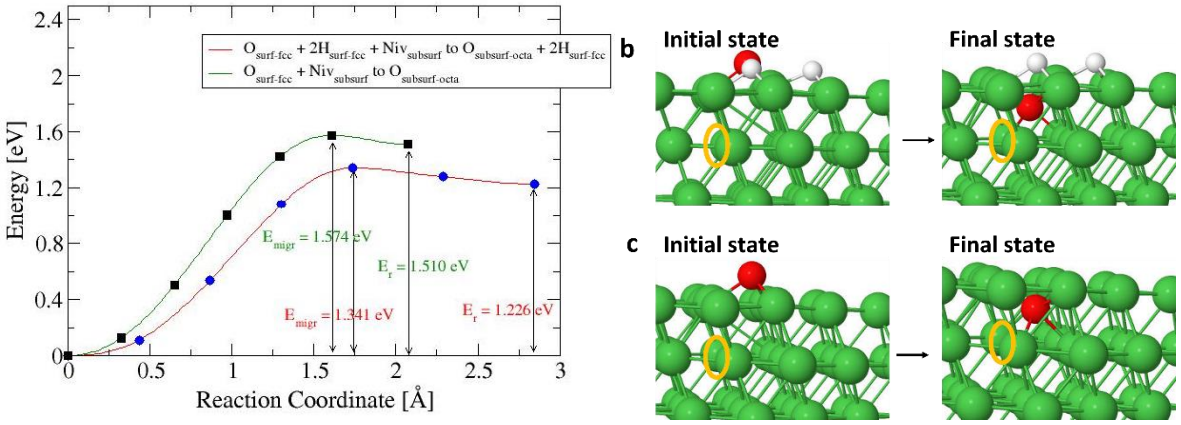

Figure 5. Migration barrier of O species diffusion into Ni(111) surface. Structures of the initial and final states (b) after $^{3}H_2O$ dissociation and (c) in bare surface. Orange circle denotes the location of Ni vacancy.

3.3.4 Diffusion of ^{2}H species into nickel surface in the presence of O surface species

In this section we studied the diffusion of two H species into Ni(111) surface in the presence of surface O and OH species. We looked at different cases.

a) One O surface species

In this subsection we looked at the diffusion of two H into Ni(111) surface after a H_2O dissociation. The first diffusion requires an energy barrier of 0.572 eV while the second requires an energy of 0.601 eV (Figure 6).

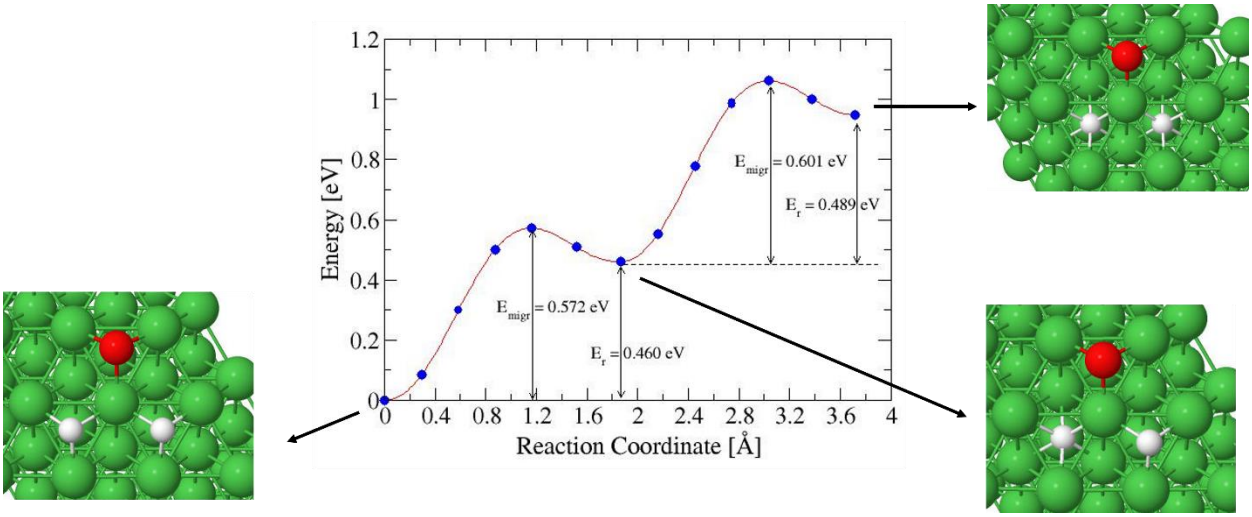

Figure 6. Migration barrier and reaction energies of two ^3H species into Ni surface after ^3H_2O dissociation.

b) Two O surface species

In this subsection we looked at the diffusion of two H species in the presence of two O surface species (Figure 7). The first H migrates into the surface with an even lower barrier and a lower reaction energy compared to the previous cases. The second H diffuses with a higher diffusion barrier of 0.643 eV and a reaction energy of 0.481 eV.

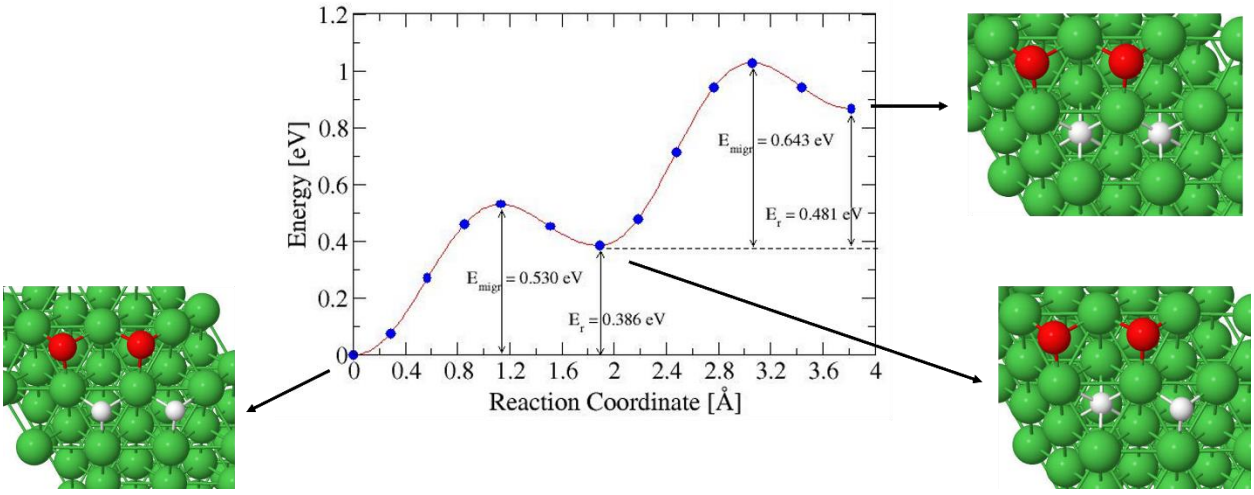

Figure 7. Migration barriers and reaction energies of two ^{3}H species in the presence of two surface O species.

c) One O and OH surface species

In this subsection we looked at the diffusion of H species in the presence of an O and OH surface species. H diffuses with a migration barrier of 0.562 eV and a reaction energy of 0.403 eV (Figure 8). This barrier is much lower than the barrier of a single H atom diffusing into a bare Ni(111) surface.

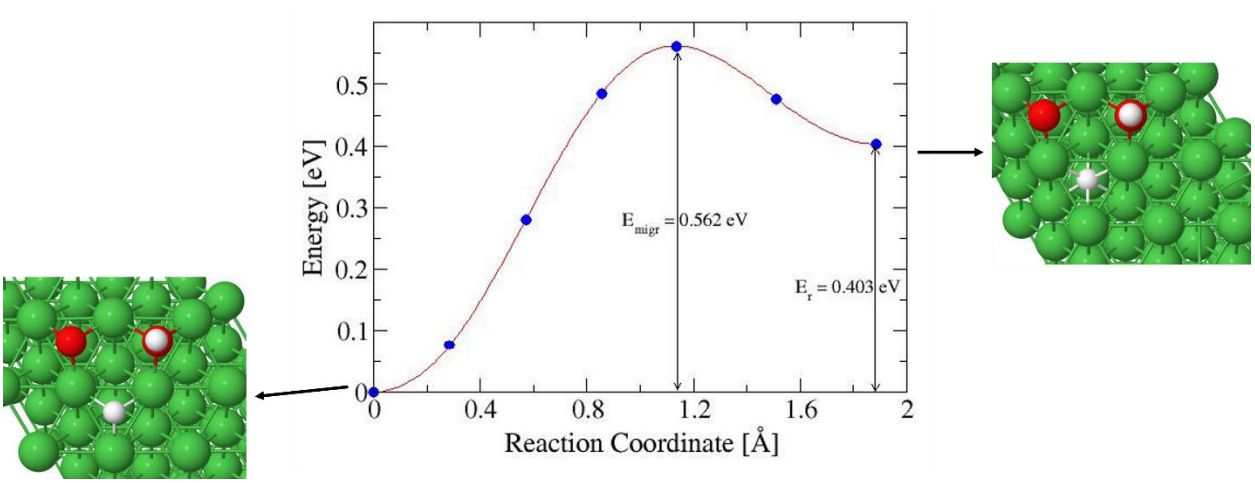

Figure 8. Migration barrier and reaction energy of the diffusion of H into the surface in the presence of O and OH species.

In all three cases, the diffusion of H species into the surface is favorable compared to that of O.

We also investigated the diffusion of H from the surface to the subsurface in the presence of an O subsurface octahedral (Figure 9). Our results reveal that H will diffuse into a subsurface octahedral with an energy barrier of 0.595 eV and an endothermic reaction energy of 0.452 eV.

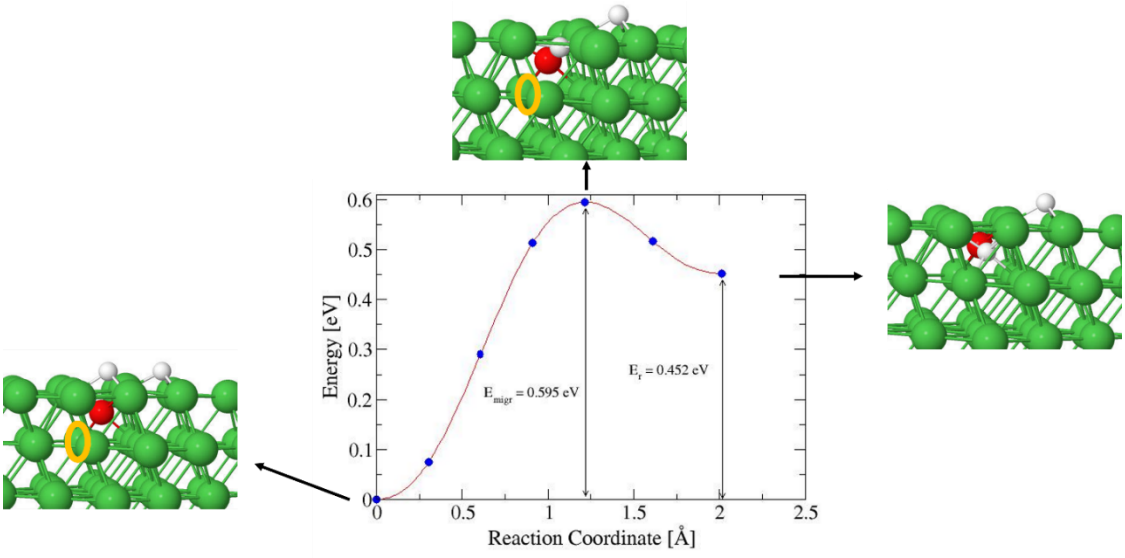

Figure 9. Migration barrier of H species into the surface in the presence of an O species in a subsurface octahedral.

3.4 Identifying the energy barrier of ^{3}H species diffusion in the Ni bulk

In this section we investigated the diffusion of H species into Ni bulk and the formation of $Ni(OH)_x$. We start with the assumption that an O species migrated into the subsurface and we study the diffusion of a H species towards O to form $Ni(OH)_x$. We looked at three different cases with the third case consisting of diffusion of OH species from the surface into the subsurface. However, OH diffusion into the surface is unfavorable. The calculations couldn't converge.

3.4.1 Case1: Formation of $Ni(OH)_x$ thru diffusion of a subsurface H species

In this case, a H species in a subsurface octahedral site is allowed to diffuse toward O to form a $Ni(OH)_x$ unit. We obtained an activation barrier of ~ 0.55 eV for the diffusion of H and formation of $Ni(OH)_x$. The reaction is endothermic by 0.125 eV (Figure 10).

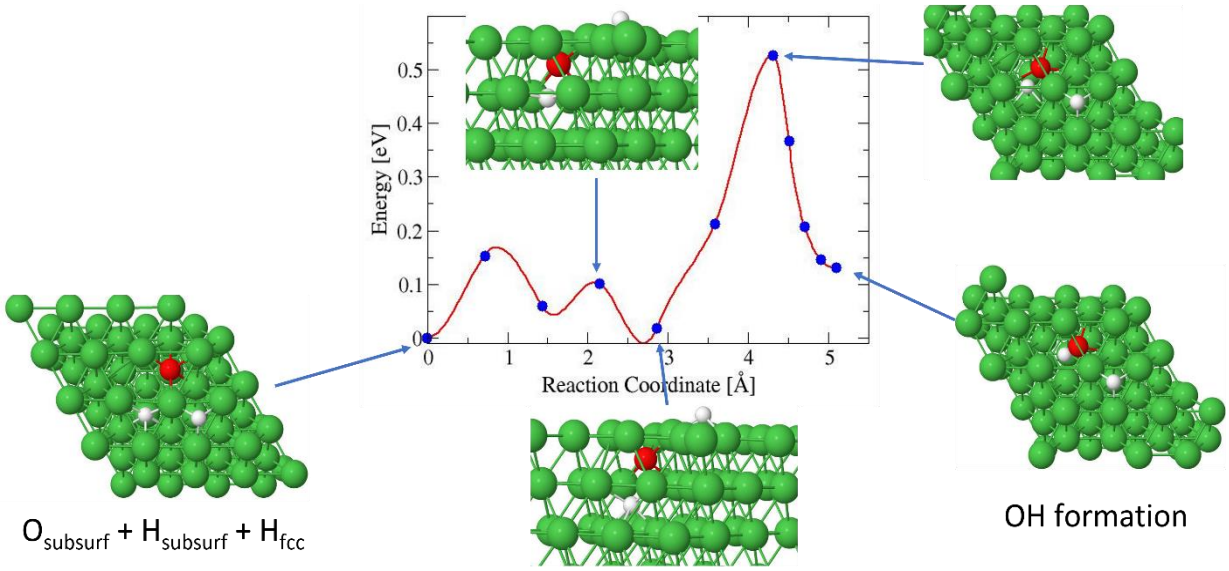

Figure 10. Diffusion barrier and diffusion pathways for subsurface H diffusion and Ni(OH)x formation.

3.4.2 Case 2: Formation of $Ni(OH)_x$ thru diffusion of a surface H species

In this case a surface H species is allowed to diffuse from a hcp site close to the subsurface O species. Our calculations show that H will first diffuse to a fcc surface site away from the subsurface O with an energy barrier of ~ 0.2 eV before migrating into a subsurface octahedral.

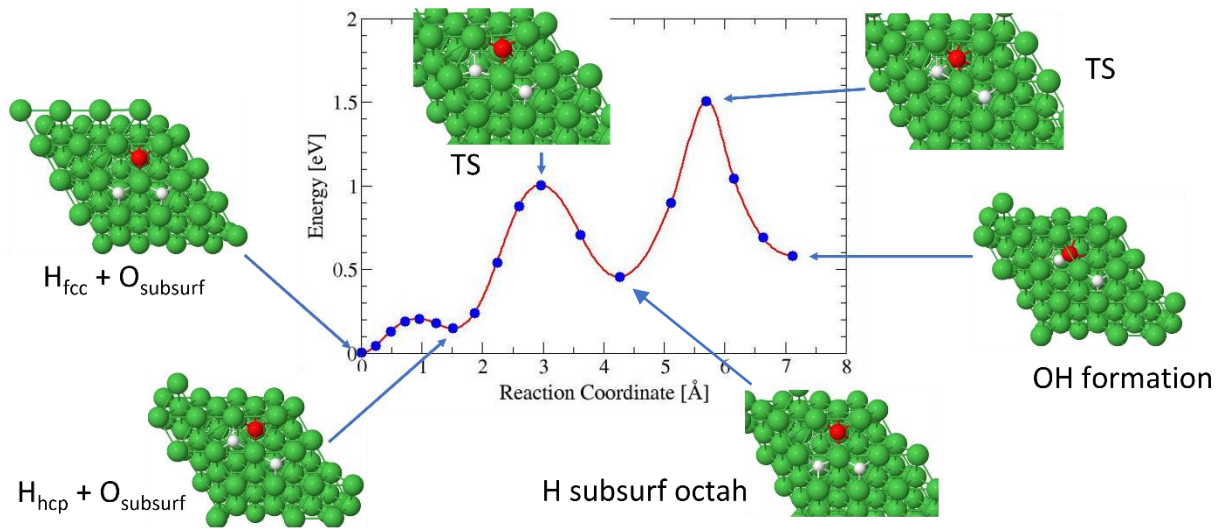

Figure 11. Diffusion barrier and transition pathways for H diffusion into surface and subsurface formation of $Ni(OH)_x$.

We also studied the diffusion of O species from a subsurface octahedral to a subsurface octahedral site. We find a diffusion barrier of less than 0.4 eV (Figure 12). However, previous work done at NETL revealed that for O to diffuse into nickel bulk requires an activation energy of at least 1.68 eV [28].

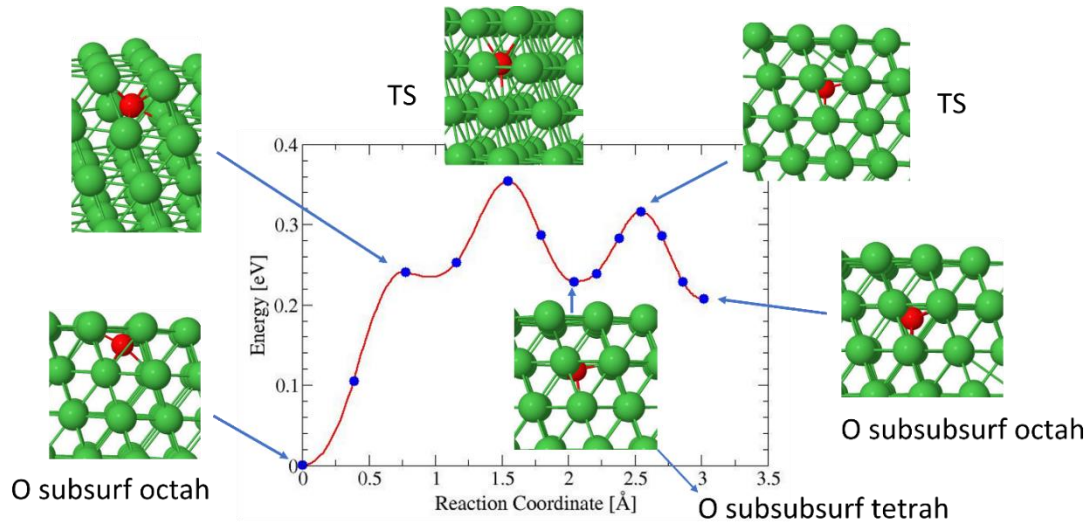

Figure 12. Diffusion barrier and reaction pathways of O species from a subsurface octahedral to a subsubsurface octahedral.

3.5 Building the interface of Ni and Zr metal

Nickel-zirconium interfaces were built using Ni(111) and Zr(0001) surfaces. Nickel bulk has a cubic structure and zirconium an hexagonal structure. Due to their different phase structures the combination of the two materials will lead to a lattice mismatch. We were able to build two stable interface models of different sizes. The larger interface with smaller lattice mismatch was modeled using a 9 × 9 supercell of Ni(111) slab containing 3 layers and a 7 × 7 supercell of Zr(0001) slab containing 2 layers. The smaller interface model with a larger lattice mismatch was built with a 5 × 5 supercell of Ni(111) slab containing also 3 layers and a 4 × 4 supercell of Zr(0001) containing two layers (Figure 13). The interface distance d_z between Ni(111) and Zr(0001) slabs were optimized and the minimum energy distance were found to be ~ 2.3 Å.

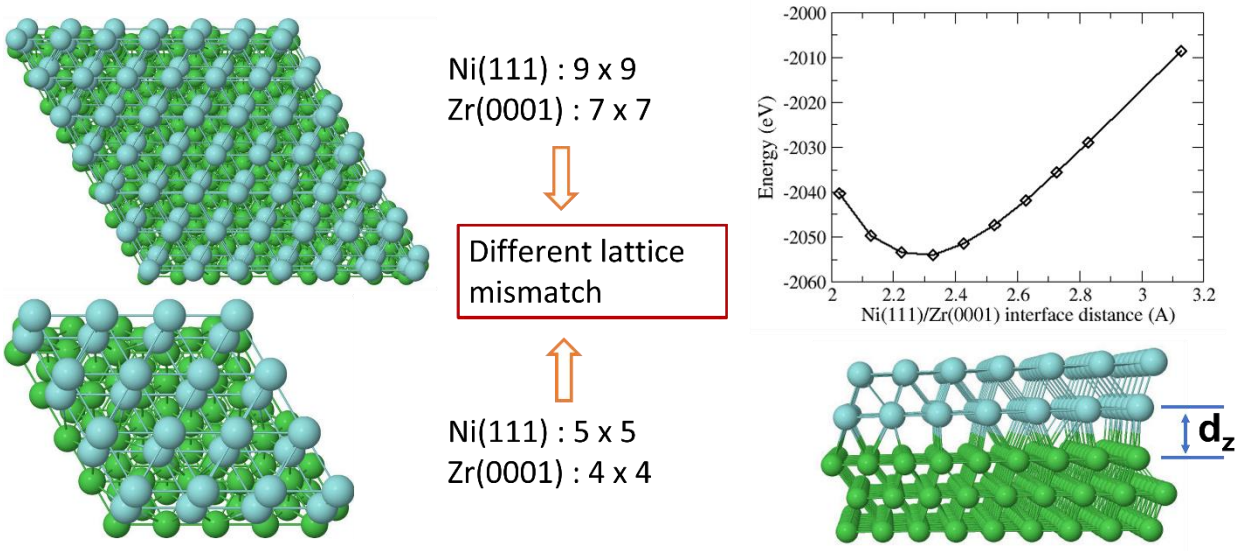

Figure 13. Interface models of Ni/Zr. Total energy for the larger supercell of Ni/Zr interface as a function of interface distance d_z.

These interface models will be used for further study (FY24) of ^{3}H species diffusion across the interface and then dissolution into Zircaloy-4 getter to form metal hydrides.

3.6 Tritium Adsorption on (100) and (001) Surfaces of Pure and Tin Defective Zirconium

3.6.1 Calculation details

To account for dispersion, the optPBE functional was coupled with the van der Waals dispersion correction (vdW-DF-optPBE).[29-33] We utilized planewave basis sets with a cutoff energy of 520 eV. The ^{3}H $1s^1$, Zr $5s^2 4d^2 5p^0$, and Sn $5s^2 5p^2$ electrons were treated explicitly in all calculations. For calculations the k-meshes were generated using the Γ-centered Monkhorst-Pack scheme, and the number of divisions among each reciprocal lattice vector was chosen such that

the product of this number with the real lattice constant was 36 Å.[34] We used the climbing-image nudged elastic band (cNEB) approach to calculate the transport barriers of ^{3}H on the surfaces and in bulk Zr. For the effect of Sn defects, only substitutional defects were considered.[35] In our calculations, the potential of the isotope ^{3}H is obtained by modifying the mass in the standard ^{1}H potential. Calculations on Zr(001) utilized a slab of 100 atoms, corresponding to four layers of 25 atoms, while calculations on Zr(100) utilized a slab of 90 atoms, corresponding to six layers of 15 atoms. Each surface system was given a vacuum space of 20.0 Å along the z-axis to prevent self-interaction. For the Zr(001), the top two layers were allowed to fully relax during calculations with ^{3}H, and for Zr(100) the top three layers were allowed to fully relax while the remaining layers were fixed to their bulk positions.

3.6.2 Determining Binding Sites

To investigate where ^{3}H bonds on the surface the possible binding locations on Zr(001) and Zr(100) and their respective energies were determined. The binding energy, E_{bind}, was calculated according to equation 10, where E_{slab+H} represents the total energy of the system with ^{3}H, E_{slab} represents the slab energy, and E_{H_2} represents the energy of the $^{3}H_2$ dimer.

$$E_{bind} = E_{slab+H} - E_{slab} - 0.5E_{H_2} \quad (10)$$

On Zr(001), both hollow sites, hexagonal close-packed (HCP) and face-centered cubic (FCC), are the most stable binding sites, and are comparable in energy. The bridge site while not as stable as the hollow sites, still had a negative binding energy, while the top site is unstable, with a positive binding energy. On Zr(100) ^{3}H can bind at upper bridge, lower bridge, and step sites.

These energies are gathered in Table 2. All Zr(100) sites have stable binding energies, but the step site is more stable than either the upper or lower bridge sites. The step site can be interpreted as sitting in a hollow site corresponding to the Miller indices (*1.5,0,-1*) in α-Zr. Both bridge sites for Zr(100) are close in energy, but the upper bridge site interacts solely with the topmost termination layer, while the lower bridge site interacts with both the uppermost and second termination layer, leading to higher energy. The sites can be visualized in Figure 14.

Table 2. Calculated binding energies for ^{3}H on Zr(001) and (100) surface sites.

Surface	**(001)**	**(001)**	**(001)**	**(001)**	**(100)**	**(100)**	**(100)**
Site(s)	**Top**	**Bridge**	**HCP**	**FCC**	**Upper Bridge**	**Lower Bridge**	**Step**
E_{bind} (eV)	**0.26**	**-0.74**	**-1.01**	**-0.99**	**-0.80**	**-0.77**	**-0.95**

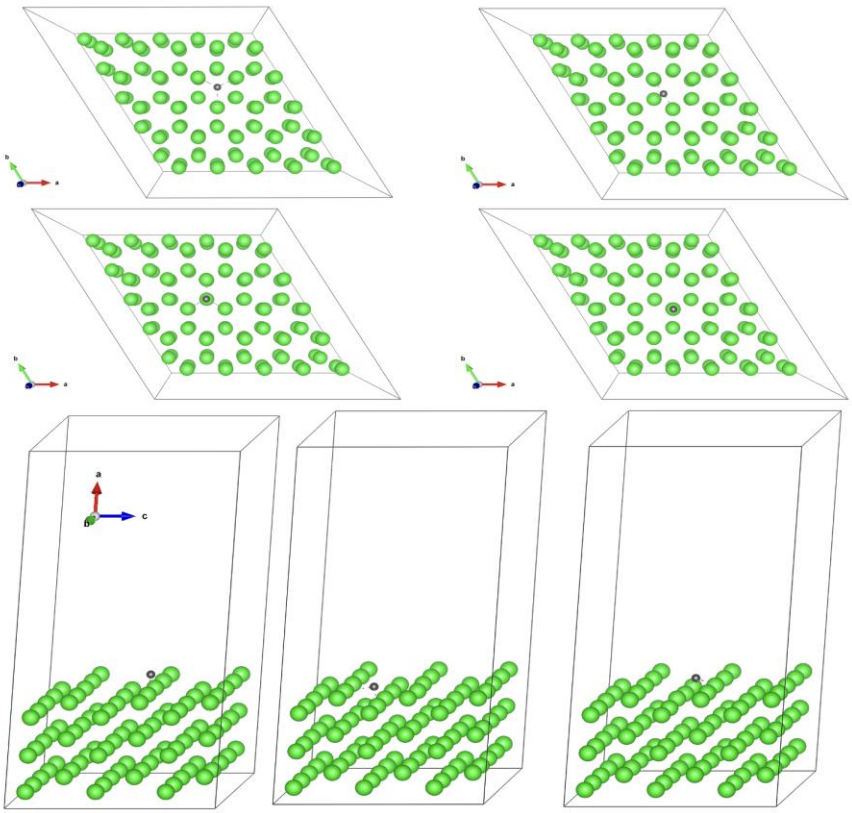

Figure 14. Top Left: FCC ^{3}H Zr(001); Top Right: Bridge ^{3}H Zr(001); Center Left: HCP ^{3}H Zr(001); Center Right: Top ^{3}H Zr(001); Bottom Left: Upper bridge ^{3}H Zr(100); Bottom Center: Lower bridge ^{3}H Zr(100) Bottom Right: Step ^{3}H Zr(100)

For both Zr (001) and (100) surfaces, multiple stable binding sites were discovered. The calculations we perform take place with minimal ^{3}H coverage, and neglect temperature. In real systems, we would expect both a larger coverage and thermal effects such as atomic motion. If the barriers between sites are sufficiently small, ^{3}H could readily transfer to different sites. This is of particular importance for transport from the surface to the subsurface, where the energy barrier to enter the bulk could be affected by the binding site. The energy barriers between the stable binding sites on the Zr surfaces were investigated. For Zr(001), ^{3}H movement away from a bridge site to either a FCC or HCP site was found to be strictly downhill. ^{3}H movement from an FCC to HCP site was found to have an energy barrier of 0.27 eV. This FCC to HCP transfer moves the ^{3}H through a bridge site, and the barrier to reach the bridge site is identical to the HCP to bridge ΔE of 0.27 eV. This strongly suggests that ^{3}H in the bridge site on the Zr(001) surface is a local maxima. This transfer is represented graphically in Figure 15.

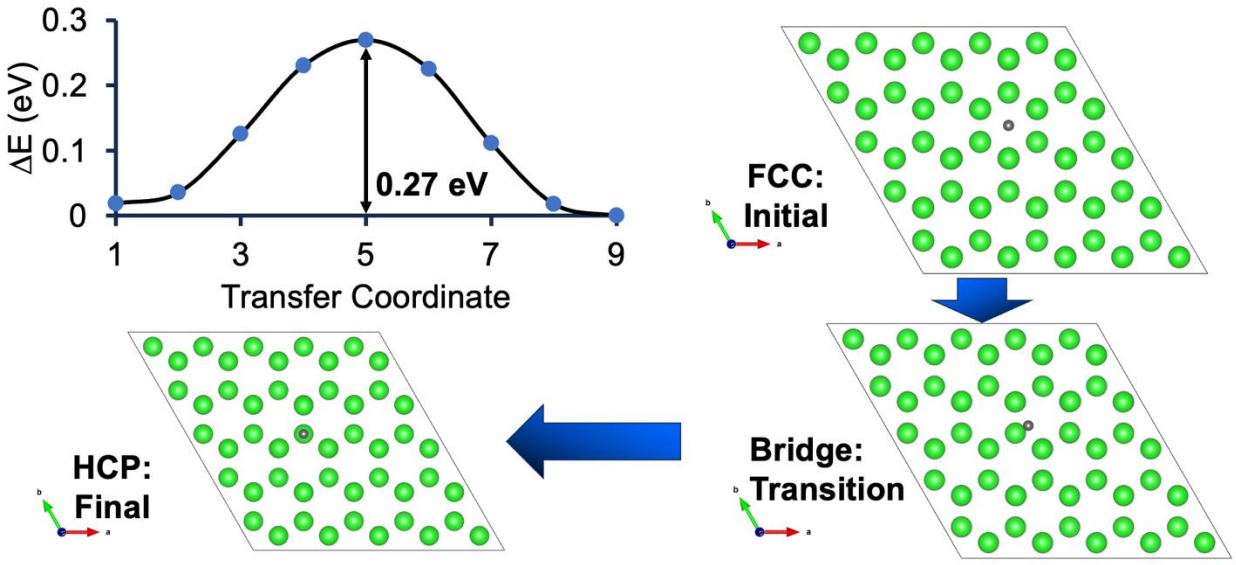

Figure 15. Energy barrier for the transfer of ^{3}H on Zr(001) from a FCC to an HCP site through a bridge site.

For Zr(100) surface, the transfer profile of ^{3}H moving from an upper bridge site to a lower bridge site, passing through a step site was calculated. While both bridge sites are higher in energy, the barrier to reach the upper bridge site from the step site is 0.15 eV, as opposed to reaching the lower bridge site from the step site requiring overcoming a barrier of 0.45 eV. This process is shown in Figure 16. A similar transfer process from a step site to a step site, shown in Figure 17, passing through a lower bridge intermediate was found to have a similar energy barrier of 0.43 eV.

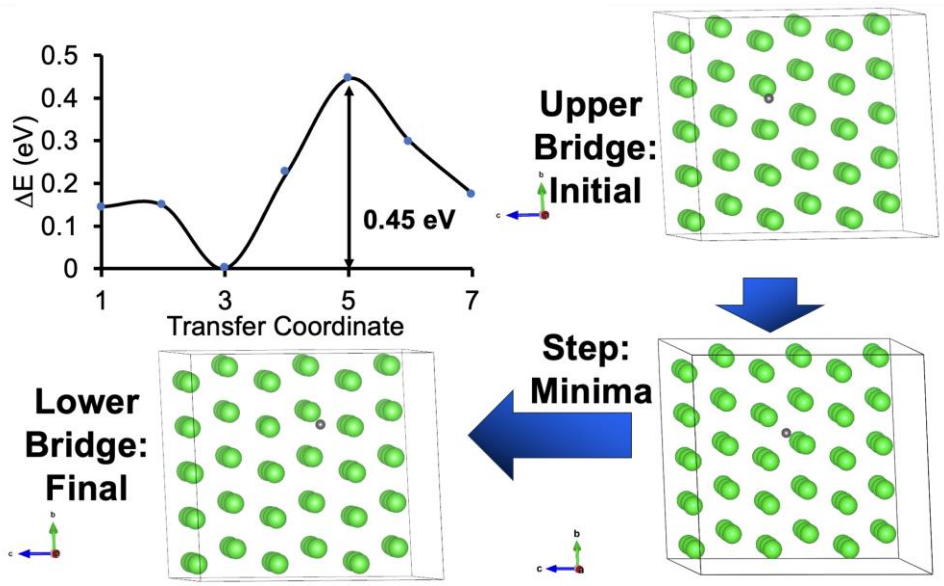

Figure 16. Energy barrier for the transfer of ^{3}H on Zr(100) from an upper to lower bridge site through a step site.

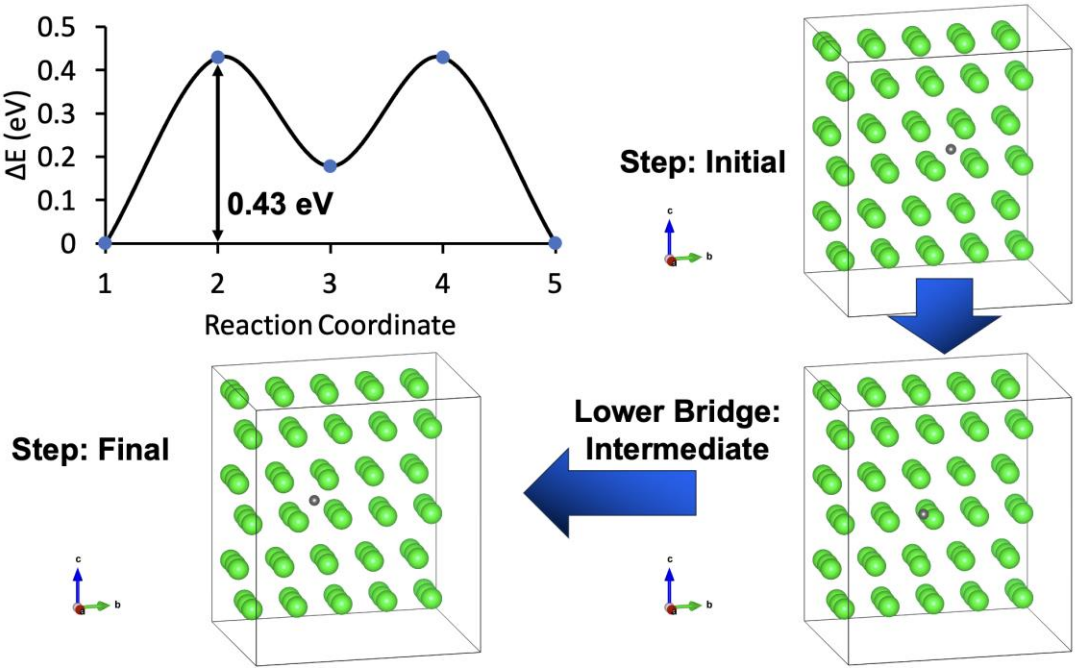

Figure 17. Energy barrier for the transfer of ^{3}H on Zr(100) from a step site to a step site passing through a lower bridge intermediate.

The binding of $^3H_2$ molecules on the Zr surfaces was also investigated, to determine if different binding sites would be favored. The dissociation of $^3H_2$ molecules on Zr surfaces is known to be a spontaneous process, thus it was expected that this would also be shown in the calculations. These binding energies are given in **Table 3**, for both Zr(001) and Zr(100). These energies were calculated according to equation 11.

$$E_{bind} = E_{slab+H} - E_{slab} - E_{H_2} \quad (11)$$

On Zr(001) $^3H_2$ dissociated when placed at HCP, FCC, and bridge sites, but remained as $^3H_2$ when on a top site. Surprisingly, for a specific orientation of $^3H_2$ on an FCC site, the $^3H_2$ dimer did not dissociate. We hypothesize that this is indicative of an inflection point on the potential energy surface for this orientation. On Zr(100) $^3H_2$ dissociated when placed at non-top sites to form two ^3H's on bridging sites. The binding energies obtained from the $^3H_2$ dissociation studies are similar to those obtained from the ^3H binding studies, taking the binding site and number of ^3H's bound into consideration.

Table 3. Calculated binding energies for $^3H_2$ in the dimer and dissociated on Zr(001) and (100) surface sites.

Surface	**(001)**	**(001)**	**(001)**	**(001)**	**(100)**	**(100)**	**(100)**
Site(s)	**Top**	**FCC**	**Bridge, HCP**	**2 HCP**	**Top**	**2 Bridge, upper layer**	**2 Bridge, lower layer**
E_{bind} (eV)	**0.14**	**0.14**	**-1.71**	**-2.03**	**-0.06**	**-1.79**	**-1.10**

3.6.3 Sn Defects on the Zr surface

Zircaloy-4 alloy consists almost entirely of Zr but contains ~1% Sn. Studies indicate that it is adequate to model Zircaloy-4 using pure Zr, however the effect of impurities can be accurately captured for large systems. Our Zr(001) and (100) surfaces contain 100 and 90 atoms, respectively. By introducing a substitutional defect, where one Zr is replaced with a Sn, we can achieve a percentage of Sn similar to that found in Zircaloy-4. Adding this defect to our Zr(001) and Zr(100) systems results in Sn percentages of 1.00% and 1.11%, respectively, in good accordance with Zircaloy-4. Sn defects were introduced to the Zr surfaces, to investigate the impact of Sn on ^{3}H binding energy. For the Zr(001) surface, when ^{3}H was relaxed in the presence of Sn, a slightly repulsive effect was observed. Both FCC and HCP ^{3}H's, when their first nearest neighbor (1NN) was Sn, would migrate from their site to the next nearest hollow site, out of interaction range with Sn. ^{3}H would relax to top and bridge sites on Sn, however neither of these sites have stable binding energy, and each is significantly higher in energy than on pure Zr. On Zr(001) surface we can compare the binding energies of -0.74 eV (bridge site, pure Zr in Table 1) to 0.24 eV (bridge site, Sn defect), and the value of 0.26 eV (top site, pure Zr in Table 1) to 1.01 eV (top site, Sn defect) to see significant increases caused by Sn. On Zr(100) surface, similar effects are observed with regards to the impact of Sn on ^{3}H binding, with numerical values provided in Table 4. When ^{3}H occupies an upper bridge site in the presence of Sn, binding becomes unfavorable. Furthermore, when ^{3}H is relaxed in the presence of Sn in a lower bridge site, the ^{3}H migrates to a step site to minimize Sn interactions. The reverse of this process occurs when ^{3}H is relaxed in the presence of Sn on a step site. The presence of Sn alone provides enough energy to cause ^{3}H to transfer sites on the surface, and no sites where ^{3}H and Sn interact favor binding, indicating strong repulsive behavior between Sn and ^{3}H. These instances of the repulsive effect of Sn on ^{3}H binding and diffusion are in agreement with published findings.[13, 36, 37]

Table 4. Calculated results of relaxing ^{3}H in the presence of Sn on Zr surfaces. Values are omitted for systems without ^{3}H – Sn interactions.

Surface	**(001)**	**(001)**	**(001)**	**(001)**	**(100)**	**(100)**	**(100)**
Initial Site	**Top**	**Bridge**	**HCP**	**FCC**	**Upper Bridge**	**Lower Bridge**	**Step**
Final Site	**Top**	**Bridge**	**FCC**	**HCP**	**Upper Bridge**	**Step**	**Lower Bridge**
On Tin?	**Yes**	**Yes**	**No**	**No**	**Yes**	**No**	**No**
E_{bind} (eV)	**1.01**	**0.24**	**--**	**--**	**0.22**	**--**	**--**

3.6.4 Surface to Subsurface transfer

While the diffusion of ^{3}H through zirconium bulk to form hydrides has been previously studied,[13, 37] the effect of surfaces on this process is unexplored. While several possible pathways exist for the transfer of ^{3}H from the surface to the bulk of Zr(001), we considered the transfer from an FCC site on the surface to an octahedral site in the bulk. The barrier for reaching a subsurface octahedral site from the FCC surface site is 0.70 eV, where the ^{3}H reaches a local minimum in the transfer process, as shown in Figure 18. From here, an energy barrier of 0.53 eV must be overcome before reaching the bulk octahedral site. The reverse transfer process, from the bulk octahedral site to the subsurface octahedral site has an energy barrier of 0.61 eV, which precisely agrees with previous calculations on the octahedral-octahedral diffusion of ^{3}H in bulk Zr.[13, 37, 38]

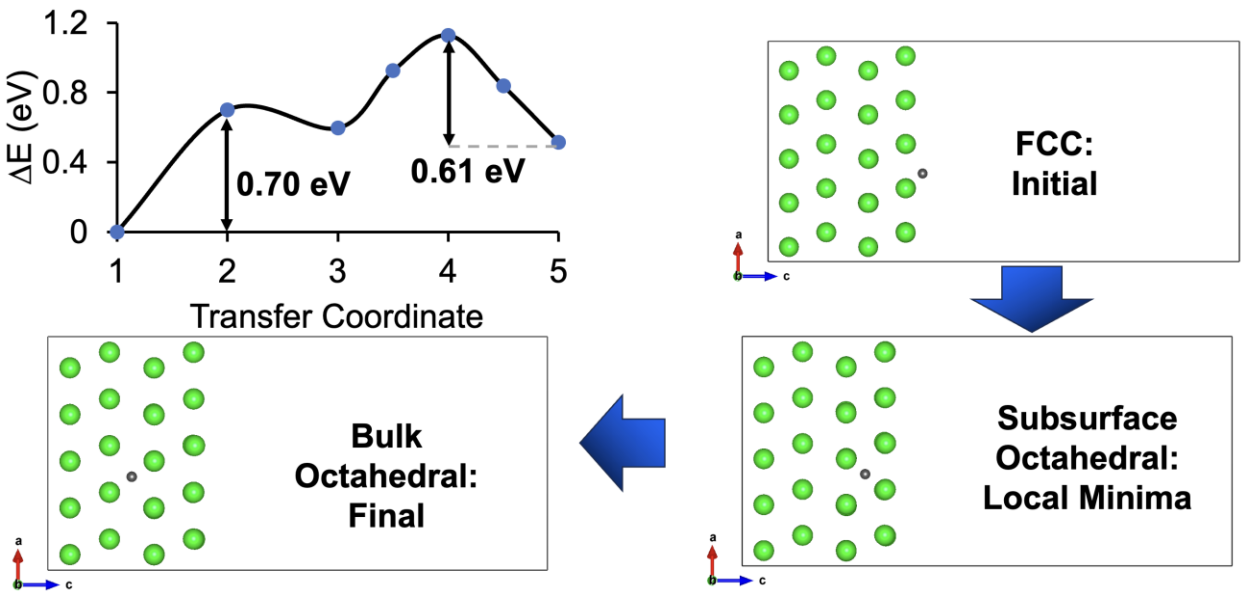

Figure 18. Energy barrier for the transfer of ^{3}H on Zr(001) from a FCC site on the surface to a subsurface octahedral site and then to a bulk octahedral site.

There are several possible paths through which ^{3}H could diffuse into Zr(100). One such path is ^{3}H moving from a step site on the surface to a tetrahedral site in the subsurface. A diagram of this process is shown in Figure 19. The energy is found to be significantly uphill for the transfer process, having to overcome a total energy barrier of 1.11 eV to reach the tetrahedral site. This large increase in energy is partly due to the Zr atom above ^{3}H moving in the *a* axis direction, away from the bulk, to accommodate ^{3}H moving into the bulk. It is likely that other pathways exist for this process, but alternative paths have not yet been calculated for this process.

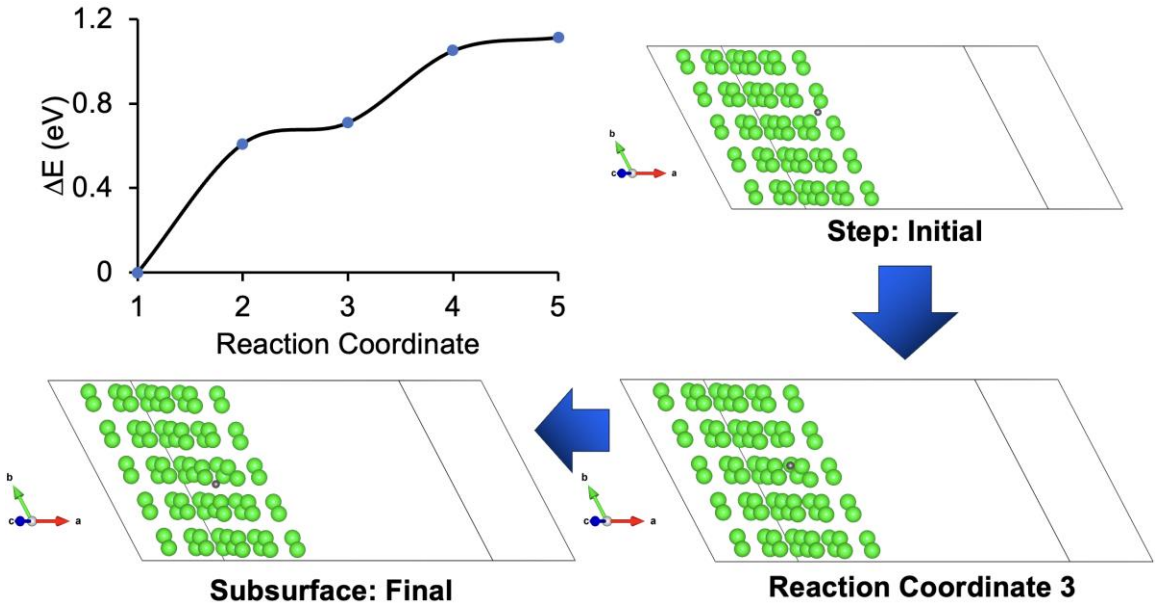

Figure 19. Energy barrier for the transfer of ^3H on Zr(100) from a step site on the surface to a subsurface tetrahedral site.

4 SUMMARY AND CONCLUSION

We explored $^3H_2$ and ^3H_2O binding sites and their dissociation on the (111) surface of Ni and concluded that the possible dissociation steps are $^3H_2O \rightarrow O^3H + {}^3H \rightarrow O + {}^3H + {}^3H$, and $^3H_2 \rightarrow {}^3H + {}^3H$. Our thermodynamical calculations and analysis show that there exists a stable chemical potential region where NiO_x or $Ni(O^3H)_x$ phase forms. $^3H_2$ and ^3H_2O species will dissociate on the surface of Ni and diffuse into the subsurface. Our diffusion barrier results predict the following:

- O will most likely stay in the Ni layer to form NiO_x or $Ni(O^3H)_x$ due to its high diffusion energy barrier compared to that of ^3H.
- Formation of NiO_x or $Ni(O^3H)_x$ phase in Ni subsurface layer is limited by O diffusion energy barrier and Ni vacancy defects.

- Only ^{3}H will pass through Ni layer to across Ni-Zircaloy-4 interface to form metal hydrides.

Better understanding of the chemical properties of zirconium are necessary to reach ultimate performance capabilities in tritium production with TPBARs. To this end we have assessed the surface chemistry of Zr interacting with ^{3}H holistically. The relative energies of ^{3}H binding sites on Zr(001) and Zr(100) were determined. The surface-surface transfer barriers for ^{3}H on these surfaces were calculated. The effect of Sn on ^{3}H was shown to have a strong repulsive effect on these surfaces. Possible paths for surface to bulk diffusion are proposed, with diffusion being more facile on the (001) surface. Our results reproduce both the spontaneous dissociation of $^{3}H_2$ on Zr and previously calculated energy profiles for the transfer of ^{3}H in bulk Zr. While surface to bulk ^{3}H transfers in the presence of Sn are still being calculated, our current work sheds light on ^{3}H diffusion mechanics and can provide future direction for Zr-based ^{3}H getters.

We also built interface models of Ni(111)/Zr(0001) and optimized them for further study (FY24) of ^{3}H species diffusion across the interface and then dissolution into Zircaloy-4 getter to form metal hydrides.

5 ACKNOWLEDGMENTS

This research is supported by the National Nuclear Security Administration (NNSA) of the U. S. Department of Energy (DOE) through the Tritium Modernization Program. We thank the National Energy Technology Laboratory (NETL) Research and Innovation Center providing Computational resources. We thank the Tritium Science Program Manager, Drs. David Senor and Andrew M. Casella (PNNL), for their excellent managemental skills and helpful comments on this work.

This research was also supported in part by an appointment with the AMMTO Summer Internships program sponsored by the U.S. Department of Energy (DOE), EERE Advanced Materials and Manufacturing Technologies Office (AMMTO). This program is administered by the Oak Ridge Institute for Science and Education (ORISE) for DOE. ORISE is managed by ORAU. All opinions expressed in this paper are the author's and do not necessarily reflect the policies and views of DOE, ORAU, or ORISE.

6 REFERENCES

[1] H.P. Paudel, Y. Duan, A First-Principles Density Function Theory Study of Tritium Diffusion in Li2ZrO3: Application for Producing Tritium, The Journal of Physical Chemistry C 122(50) (2018) 28447-28459.

[2] H.P. Paudel, Y.-L. Lee, D.J. Senor, Y. Duan, Tritium Diffusion Pathways in γ-LiAlO2 Pellets Used in TPBAR: A First-Principles Density Functional Theory Investigation, The Journal of Physical Chemistry C 122(18) (2018) 9755-9765.

[3] Y.-L. Lee, J. Holber, H.P. Paudel, D.C. Sorescu, D.J. Senor, Y. Duan, Density functional theory study of the point defect energetics in γ-LiAlO2, Li2ZrO3 and Li2TiO3 materials, Journal of Nuclear Materials 511 (2018) 375-389.

[4] Y. Duan, D.C. Sorescu, W. Jiang, D.J. Senor, Theoretical study of the electronic, thermodynamic, and thermo-conductive properties of γ-LiAlO2 with 6Li isotope substitutions for tritium production, Journal of Nuclear Materials 530 (2020) 151963.

[5] T. Jia, D.J. Senor, Y. Duan, First-principles study of the tritium reaction and diffusion on the γ-LiAlO2 (1 0 0) surface with carbon impurity, Computational Materials Science 181 (2020) 109748.

[6] T. Jia, D.J. Senor, Y. Duan, Tritium species diffusion on and desorption from γ-LiAlO2 (100) surface: A first-principles investigation, Journal of Nuclear Materials 540 (2020) 152394.

[7] T. Jia, D.J. Senor, Y. Duan, Trapping and recombination of tritium in lithium vacancy of the γ-LiAlO2 (100) surface: A first-principles study, Applied Surface Science Advances 5 (2021) 100114.

[8] T. Jia, D.J. Senor, Y. Duan, First-principles study of the surface properties of LiAl5O8: Stability and tritiated water formation, Journal of Nuclear Materials 555 (2021) 153111.

[9] T. Jia, Z. Zeng, H. Paudel, D.J. Senor, Y. Duan, First-principles study of the surface properties of γ-LiAlO2: Stability and tritium adsorption, Journal of Nuclear Materials 522 (2019) 1-10.

[10] H.P. Paudel, D.J. Senor, Y. Duan, Effects of carbon impurity on tritium diffusion and helium formation in γ-LiAlO2 pellets: A first-principles study, Computational Materials Science 193 (2021) 110419.

[11] C.M. Andolina, W.A. Saidi, H.P. Paudel, D.J. Senor, Y. Duan, Hydrogen localization and cluster formation in α-Zr from first-principles investigations, Computational Materials Science 209 (2022) 111384.

[12] T. Jia, H.P. Paudel, D.J. Senor, Y. Duan, First-principles studies of the concentration-dependent tritium diffusion in the zirconium hydrides with and without Sn impurity, Computational Materials Science 203 (2022) 111158.

[13] H.P. Paudel, T. Jia, W.A. Saidi, D.J. Senor, A.M. Casella, Y. Duan, Study of Tritium Diffusivity in Pure and Sn-Defective Zr: A First-Principles Density Functional Theory Approach, The Journal of Physical Chemistry C 127(26) (2023) 12435-12443.

[14] J. Carrasco, A. Hodgson, A. Michaelides, A molecular perspective of water at metal interfaces, Nature Materials 11(8) (2012) 667-674.

[15] K. Christmann, R.J. Behm, G. Ertl, M.A. Van Hove, W.H. Weinberg, Chemisorption geometry of hydrogen on Ni(111): Order and disorder, The Journal of Chemical Physics 70(9) (2008) 4168-4184.

[16] G. Kresse, J. Furthmuller, Efficiency of ab-initio total energy calculations for metals and semiconductors using a plane-wave basis set, Comp Mater Sci 6(1) (1996) 15-50.

[17] G. Kresse, J. Furthmüller, Efficient iterative schemes for ab initio total-energy calculations using a plane-wave basis set, Physical Review B 54(16) (1996) 11169-11186.

[18] G. Kresse, J. Hafner, Ab initio molecular dynamics for liquid metals, Physical Review B 47(1) (1993) 558-561.

[19] P.E. Blöchl, Projector augmented-wave method, Phys Rev B 50(24) (1994) 17953-17979.
[20] G. Kresse, D. Joubert, From ultrasoft pseudopotentials to the projector augmented-wave method, Phys Rev B 59(3) (1999) 1758-1775.
[21] J.P. Perdew, K. Burke, M. Ernzerhof, Generalized Gradient Approximation Made Simple, Physical Review Letters 77(18) (1996) 3865-3868.
[22] G. Henkelman, B.P. Uberuaga, H. Jónsson, A climbing image nudged elastic band method for finding saddle points and minimum energy paths, The Journal of Chemical Physics 113(22) (2000) 9901-9904.
[23] L. Zhu, C. Liu, X. Wen, Y.-W. Li, H. Jiao, Molecular or dissociative adsorption of water on clean and oxygen pre-covered Ni(111) surfaces, Catalysis Science & Technology 9(1) (2019) 199-212.
[24] M. Shirazi, A. Bogaerts, E.C. Neyts, A DFT study of H-dissolution into the bulk of a crystalline Ni(111) surface: a chemical identifier for the reaction kinetics, Physical Chemistry Chemical Physics 19(29) (2017) 19150-19158.
[25] J. Heyd, G.E. Scuseria, M. Ernzerhof, Hybrid functionals based on a screened Coulomb potential, The Journal of Chemical Physics 118(18) (2003) 8207-8215.
[26] L.-F. Huang, J.M. Rondinelli, Electrochemical phase diagrams of Ni from ab initio simulations: role of exchange interactions on accuracy, Journal of Physics: Condensed Matter 29(47) (2017) 475501.
[27] A. Jain, S.P. Ong, G. Hautier, W. Chen, W.D. Richards, S. Dacek, S. Cholia, D. Gunter, D. Skinner, G. Ceder, K.A. Persson, Commentary: The Materials Project: A materials genome approach to accelerating materials innovation, APL Materials 1(1) (2013).
[28] H.Z. Fang, S.L. Shang, Y. Wang, Z.K. Liu, D. Alfonso, D.E. Alman, Y.K. Shin, C.Y. Zou, A.C.T. van Duin, Y.K. Lei, G.F. Wang, First-principles studies on vacancy-modified interstitial diffusion mechanism of oxygen in nickel, associated with large-scale atomic simulation techniques, Journal of Applied Physics 115(4) (2014).
[29] J. Klimeš, D.R. Bowler, A. Michaelides, Chemical accuracy for the van der Waals density functional, J Phys Condens Matter 22(2) (2010) 022201.
[30] J. Klimeš, D.R. Bowler, A. Michaelides, Van der Waals density functionals applied to solids, Phys Rev B 83(19) (2011) 195131.
[31] M. Dion, H. Rydberg, E. Schröder, D.C. Langreth, B.I. Lundqvist, Van der Waals Density Functional for General Geometries, Physical Review Letters 92(24) (2004) 246401.
[32] T. Thonhauser, V.R. Cooper, S. Li, A. Puzder, P. Hyldgaard, D.C. Langreth, Van der Waals density functional: Self-consistent potential and the nature of the van der Waals bond, Phys Rev B 76(12) (2007) 125112.
[33] G. Román-Pérez, J.M. Soler, Efficient Implementation of a van der Waals Density Functional: Application to Double-Wall Carbon Nanotubes, Physical Review Letters 103(9) (2009) 096102.
[34] H.J. Monkhorst, J.D. Pack, Special Points for Brillouin-Zone Integrations, Phys. Rev. B 13(12) (1976) 5188-5192.
[35] C. Freysoldt, P. Rinke, M. Scheffler, Controlling Polarization at Insulating Surfaces: Quasiparticle Calculations for Molecules Adsorbed on Insulator Films, Physical Review Letters 103(5) (2009) 056803.
[36] Y. Zhang, C. Jiang, X. Bai, Anisotropic hydrogen diffusion in α-Zr and Zircaloy predicted by accelerated kinetic Monte Carlo simulations, Scientific Reports 7 (2017) 41033.
[37] T. Jia, H.P. Paudel, D.J. Senor, Y.H. Duan, First-principles studies of the concentration-dependent tritium diffusion in the zirconium hydrides with and without Sn impurity, Comp Mater Sci 203 (2022).

[38] C.M. Andolina, W.A. Saidi, H.P. Paudel, D.J. Senor, Y. Duan, Hydrogen localization and cluster formation in alpha-Zr from first-principles investigations, Comp Mater Sci 209 (2022) 111384.